






Article

Hydrogen Spillover in Tungsten Oxide Bronzes as Observed by Broadband Neutron Spectroscopy

Erwin Lalik ¹, Stewart F. Parker ², Gavin Irvine ³, Ivan da Silva ², Matthias Josef Gutmann ², Giovanni Romanelli ⁴, Kacper Druzbicki ^{5,6}, Robert Kosydar ¹ and Matthew Krzystyniak ^{2,*}

¹ Jerzy Haber Institute of Catalysis and Surface Chemistry, Polish Academy of Sciences, ul. Niezapominajek 8, 30-239 Cracow, Poland; nclalik@cyf-kr.edu.pl (E.L.); robert.kosydar@ikifp.edu.pl (R.K.)

² ISIS Facility, Rutherford Appleton Laboratory, Chilton, Didcot OX11 0QX, UK; stewart.parker@stfc.ac.uk (S.F.P.); ivan.da-silva@stfc.ac.uk (I.d.S.); matthias.gutmann@stfc.ac.uk (M.J.G.)

³ School of Chemistry, University of St. Andrews, St. Andrews, Fife KY16 9ST, UK; gji4@st-andrews.ac.uk

⁴ Dipartimento di Fisica and NAST Centre, Università degli Studi di Roma Tor Vergata, 00133 Rome, Italy; giovanni.romanelli@uniroma2.it

⁵ Materials Physics Center, CSIC-UPV/EHU, Paseo de Manuel Lardizabal 5, 20018 Donostia-San Sebastian, Spain; kacper.druzbicki@ehu.eus

⁶ Centre of Molecular and Macromolecular Studies, Polish Academy of Sciences, 90-363 Lodz, Poland

* Correspondence: matthew.krzytyniak@stfc.ac.uk; Tel.: +44-7825307959

Abstract: Hydrogen spillover is an elusive process, and its characterization, using experimental probes and ab initio modeling, poses a serious challenge. In this work, the nuclear quantum dynamics of hydrogen in a palladium-decorated cubic polymorph of tungsten oxide, Pd/cWO₃, are characterized by the technique of neutron Compton scattering augmented by ab initio harmonic lattice modeling. The deeply penetrating nature of the neutron scattering process, the lack of spectroscopic selection rules, the inherent high sensitivity to hydrogen, the high energy and momentum resolution for hydrogen, and the mass selectivity of the technique render the neutron Compton scattering a very potent and unique tool for investigating the local dynamics of hydrogen species in bulk matrices. The total neutron Compton scattering response of hydrogen is described in terms of the hydrogen momentum distribution. The distribution is deconvoluted under the assumption of three pools of hydrogen with distinctly different nuclear quantum dynamical behavior: (i) hydrogen-terminated beta-palladium hydride, (ii) hydrogen in acid centers (OH⁺ groups) on the surface of the cubic phase of tungsten oxide, and (iii) quasi-free atomic hydrogen inside the saturated hydrogen bronze resulting from the spillover process. The ab initio modeling of lattice dynamics yields theoretical predictions for the values of the widths of proton momentum distributions in the first two hydrogen pools, which allows for obtaining the contribution and the width of the momentum distribution of the quasi-free atomic hydrogen resulting from the hydrogen spillover process. The analysis reveals that the local binding strength of the quasi-free hydrogen is characterized by the values of nuclear momentum distribution width, nuclear kinetic energy, and force constant of the underlying potential of the mean force close to those of free, unconstrained hydrogen atomic species in a gas of non-interacting particles described by the Maxwell–Boltzmann distribution. Moreover, this picture of the local dynamics of the quasi-free hydrogen is consistent with the proton polaron model of hydrogen-induced coloration of bulk hydrogenated WO₃.

Keywords: heterogeneous catalysis; hydrogen bronzes; hydrogen spillover; neutron Compton scattering; nuclear quantum effects



Citation: Lalik, E.; Parker, S.F.; Irvine, G.; da Silva, I.; Gutmann, M.J.; Romanelli, G.; Druzbicki, K.; Kosydar, R.; Krzystyniak, M. Hydrogen Spillover in Tungsten Oxide Bronzes as Observed by Broadband Neutron Spectroscopy. *Energies* **2023**, *16*, 5496. <https://doi.org/10.3390/en16145496>

Academic Editor: Adam Revesz

Received: 29 April 2023

Revised: 27 June 2023

Accepted: 7 July 2023

Published: 20 July 2023



Copyright: © 2023 by the authors. Licensee MDPI, Basel, Switzerland. This article is an open access article distributed under the terms and conditions of the Creative Commons Attribution (CC BY) license (<https://creativecommons.org/licenses/by/4.0/>).

1. Introduction

The individual interactions of atomic hydrogen species with oxygen atoms within the crystal lattice of transition metal oxides result in a range of collective phenomena involving, in equal measure, the hydrogen and oxygen sub-lattices. The ability of atomic

hydrogen to pervade the crystal structures of transition metal oxides and to form a sub-lattice within those structures paves the way for the systems such as Pd/H_xMoO₃ or Pd/H_xWO₃ (the so-called hydrogen bronzes) to be applied as heterogeneous catalysts [1], gas sensors, or hydrogen storage materials [2–4]. Not only is the atomic hydrogen amply accommodated, but also the bronze formation gives rise to certain collective phenomena, such as the substantial mobility of hydrogen species within the host lattice and changes in the electric conductivity of the host induced by the hydrogen intercalation. These phenomena, and their underlying dynamics, involve an interaction between the hydrogen sub-lattice and the oxygen sub-lattice, which are fundamental to the understanding of the properties of the bronzes. Hydrogen mobility is key to the excellent performance of the Pd-decorated bronzes as hydrogenation catalysts at ambient conditions [1,5–12]. The efficient transport of hydrogen species through the bulk toward the catalyst surface enhances the catalytic performance of the bronze. It makes it possible for the oxide to act not merely as a support for the Pd metallic particles but, at the same time, also to play a more active role as a reservoir of active hydrogen species facilitating their eventual insertion into an organic molecule.

The presence of noble metals greatly facilitates the intercalation of hydrogen species in the host lattices of the transition metal oxides. Although simple exposure of the oxide to gaseous hydrogen is usually sufficient for the bronze to be formed, since the bond energy of the H₂ molecule is as high as 440 kJ/mol, it is a slow process without an extra component activating the molecular hydrogen. On the other hand, doping the oxide surface with noble metals such as Pd enables the bronze formation to be completed under a relatively small partial pressure of H₂ and at room temperature (RT) rather than at ca. 300 °C required otherwise. The role of the metallic Pd is to adsorb molecular hydrogen dissociatively at low temperatures. Afterward, the atomic hydrogen species spill over from the metallic nanoparticles onto the oxide surface. Eventually, they penetrate the oxide bulk and are accommodated within the crystal lattice. Despite the large bonding energy of molecular hydrogen, the formation of bronze from Pd/WO₃ is an exothermic process (cf. Figure 1) [1]. The figure represents the differential heats of sorption for the intercalation of hydrogen into two Pd-doped WO₃ polymorphs. Both curves show marked maxima, indicative of a kind of collective phenomena involved in the hydrogen uptake, which are reflected in the rate of heat evolution.

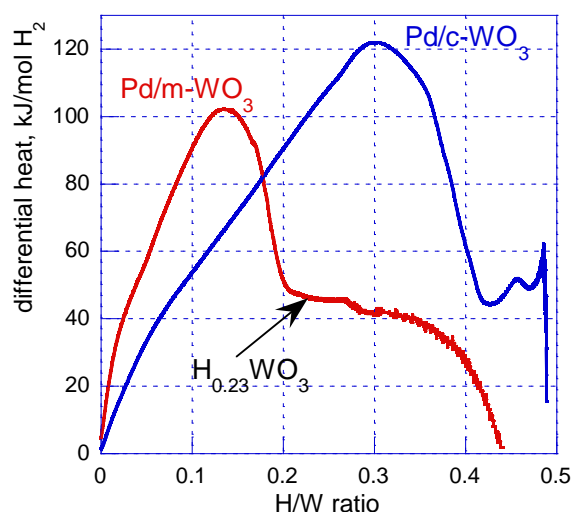


Figure 1. Differential heat of sorption of hydrogen in the monoclinic (red line) and cubic (blue line) WO₃ host lattice. The arrow marks the point of the H/W ratio corresponding to the H_{0.23}WO₃ stoichiometry. For details of the Pd/mWO₃ preparation, see Ref. [1].

Tungsten trioxide is a popular n-type semiconductor with promising electrochemical properties, a high surface area, a small pore-size distribution, with several exciting

chemical and physical properties, which have made it an appropriate material for various applications such as catalysts, gas sensors, and energy storage applications [13]. Tungsten trioxide can form several polymorphs. The RT-stable polymorph of WO_3 is monoclinic ($\text{P}2_1/\text{n}$) [14]. Monoclinic tungsten trioxide has several technologically relevant applications. The monoclinic phase was recently used to produce mesoporous tungsten oxide nano bricks (WO_3 NBs), demonstrating high sensitivity and selectivity for liquid ammonia and humidity sensing at RT [13]. Photoanodes, composed of a monoclinic WO_3 nanorod core encapsulated with a rutile TiO_2 nanoparticles shell, have recently been developed for dye-sensitized solar cells (DSSCs) of very high power conversion efficiency [15].

Monoclinic tungsten trioxide is usually used as the starting material for bronze synthesis. However, the process has stepwise kinetics [1,14,16], as depicted in Figure 1, which shows that the heat evolution drops dramatically after the H/W ratio reaches the value of ca. 0.2. In practice, it means that the latter stage may be painfully slow. On the other hand, cubic WO_3 has been found to persist when cooled to RT in spite of actually being formed at ca. 250 °C [17–20]. Recently, a method for reproducible production of the cWO_3 polymorph decorated with metallic Pd nanoparticles has been developed [21]. The method uses H_2WO_4 as a starting material to be decorated with Pd nanoparticles and then transforms the so-prepared Pd/ H_2WO_4 into the final Pd/ cWO_3 polymorph. On exposure to hydrogen at RT, such Pd/ cWO_3 material can be intercalated to reach a stoichiometry close to the $\text{H}_{0.53}\text{WO}_3$ bronze, similar to that obtained on hydrogen exposure of the stable Pd/ mWO_3 under the same conditions. However, gas flow micro-calorimetry has revealed that the total heat of sorption and the kinetics of heat evolution accompanying the intercalation differ significantly between Pd/ mWO_3 and Pd/ cWO_3 (cf. Figure 1). Crucially, it has single-step kinetics, and the process is much faster. Therefore, we propose using the Pd/ cWO_3 as the starting material for the formation of the $\text{H}_{0.53}\text{WO}_3$ bronze.

In this work, we use the unique neutron instrument, VESUVIO thermal-to-epithermal neutron station, installed at the ISIS Neutron and Muon Source at the STFC Rutherford Appleton Laboratory in the UK [22–28] to study the nuclear quantum dynamics of hydrogen in a palladium-decorated cubic polymorph of tungsten oxide, WO_3 (cWO_3). We employ the technique of neutron Compton scattering (NCS) in combination with neutron transmission (NT), both of which are readily available at VESUVIO. Our primary motivation is to characterize the nuclear quantum behavior of hydrogen species in terms of NCS-specific observables [24,25,29,30], including the widths of the nuclear momentum distributions (NMD widths), nuclear kinetic energy (NKE) values of hydrogen, and the magnitudes of the force constants (FCs) of the underlying potentials of the mean force. We characterize the total NCS response of hydrogen in the system under investigation in terms of three pools of hydrogen with distinctly different nuclear quantum dynamical behavior: (i) hydrogen-terminated beta-palladium hydride, (ii) hydrogen in acid centers (OH^+ groups) on the surface of the cubic phase of tungsten oxide, and (iii) quasi-free atomic hydrogen inside the saturated hydrogen bronze resulting from the spillover process.

For the modern analysis of neutron spectroscopic results in solid-state systems and molecules, ab initio modeling is indispensable. In this work, following our successful protocol [24,25,31–43], we employ ab initio density functional theory (DFT)—based on harmonic lattice dynamics (HLD) simulations to predict the values of NMD widths, NKE, and FCs for the first two hydrogen pools. Fixing the NCS response of the first two hydrogen pools in the non-linear constrained fitting of the total NMD of the entire system enables us to obtain the values of the NCS observables for the most elusive and challenging to model theoretically, namely the quasi-free proton pool resulting from the hydrogen spillover process [44–54]. Crucial to this process of elucidation of nuclear dynamical properties are three factors: (i) the mass selective nature of the NCS technique, (ii) the undisputed success of the DFT-based HLD approach in modeling this NCS-specific information [24,25,31–43], and (ii) the very high energy and momentum resolution of VESUVIO in the case of hydrogen NCS spectra [22–28].

In recent years, there has been an upsurge in modeling the phenomenon of hydrogen spillover theoretically using DFT [55–81]. Many phenomena have been studied, including the correlation between charge transfer and structural properties, hydrogen adsorption energies, magnetic behavior, and electronic properties [55,81], formation energy, hydrogen dissociation capacity [57], H atom binding ability, and H₂ dissociation barriers [59], strategies for the reduction of H migration barrier in hydrogen spillover [62], preferred hydrogen adsorption sites [65], the role of the surface Brønsted acid sites (hydroxyl groups) in initiating H spillover [66], minimum-energy paths of H migration from a Pt catalyst to a WO₃ surface and bulk [81], to name but a few. However, DFT studies involving the calculation of vibrational densities of states relevant to the spillover process are very rare [60,79,80]. Similarly, indirect identification of vibrational or electronic structure signatures of atomic hydrogen insertion in bulk metal-oxide systems is rare and controversial [82–88]. In the case of hydrogen-intercalated tungsten trioxide, H_xWO₃, optical and electrical changes observed upon insertion of hydrogen into WO₃ are controversially debated within two main models [82]. In the first model, hydrogen is intercalated into WO₃ and remains there, most likely as hydroxide. The corresponding electron forms a conducting phase [84,86]. In the second model, hydrogen can form water with oxygen from WO₃ and form a substoichiometric crystal [88]. The corresponding oxygen vacancies are filled with electrons. The loss of oxygen from the lattice induces distortions, leading to electron localization, described by an electron polaron model [85]. It is believed that the origin of the controversy stems from the inability to detect and characterize hydrogen in the oxide [82]. To this end, this work presents a robust experimental and modelling protocol that can be used to elucidate the nuclear chemical dynamics of hydrogen in the hydrogenated palladium-decorated cubic polymorph of tungsten oxide, Pd/cWO₃, both in the context of the spillover phenomenon and the hydrogenation of bulk metal-oxide systems.

2. Materials and Methods

2.1. Catalyst Preparation

The catalyst preparation procedure followed our previous work on the role of hydrogen bronzes in the hydrogenation of different reagents [1,6,7]. The catalyst with Pd loading of 4 wt% was prepared by impregnation of the tungstic acid H₂WO₄ (Aldrich) with palladium (II) acetate Pd(OCOCH₃)₂ (Sigma-Aldrich) solution in acetone (0.05 mol/dm³) carried out on a water bath (ca. 45 °C) up to evaporation of liquid. The obtained powder was dried in air for 24 h and reduced at atmospheric pressure with 5% H₂ in Ar (gas stream flow of 15 cm³/min) at 250 °C for 3 h. After the high-temperature reduction step, metallic palladium deposited on a cubic tungsten oxide catalyst was obtained. The final material was stored in air.

2.2. Characterization

The sample characterization followed the protocol from our previous work [1,6,7]. The content of Pd in the fresh and spent catalysts was determined by X-ray fluorescence spectroscopy (XRF) with a series of Pd/WO₃ samples with known Pd content used as calibrants. A microscale gas flow-through microcalorimeter (FMC) has been used for the microcalorimetric measurements. The instrument measures the rate of heat evolution accompanying the exposure of Pd/WO₃ to a flow of hydrogen-containing gas mixture at isothermal conditions. Concurrently, it also detects the rate of hydrogen uptake using the thermoconductivity detector downstream. The principles of operation of FMC, as well as its use for the Pd-assisted formation of the transition metal hydrogen bronzes, have been described in detail in Refs. [89] and [6], respectively.

2.3. Neutron Scattering Measurements at VESUVIO

The experimental setup was inspired by neutron quasielastic and diffraction experiments on proton-conducting samples performed at ISIS in recent years [90]. A pure sample was pressed into a 25 mm diameter pellet of 3 mm thickness and loaded into St Andrews

in situ cell (see Figure S1 in Ref. [90]). The original cell design was adapted for neutron experiments at ISIS. The outer cell material is quartz for a low background due to its low neutron cross-section values. The cell can run to temperatures of 1200 °C and allows for flowing oxidative or reductive gas atmospheres. The experiments were performed at RT under continuous gas flow, and the gas atmosphere was composed of 80% helium and 20% hydrogen, based on our previous microcalorimetric work [1,6,7]. The cell was placed inside a RAL 4 furnace. With the help of the ISIS Pressure and Furnace Team, the cell was leak tested, evacuated, and placed inside the VESUVIO spectrometer. The sample in the cell was evacuated using a turbo-molecular pump which was backed by a dual-stage rotary pump with a zeolite trap to avoid back-diffusion of oil and other potential molecular contaminants. The hydrogen uptake was monitored by capacitive pressure transducers. During the exposure of Pd/WO₃ to a flow of hydrogen at isothermal conditions on VESUVIO, the stoichiometry of the sample increased from Pd/cWO₃ towards Pd/H_{0.53}WO₃ bronze. The neutron Compton peak analysis in the time-of-flight domain confirmed this final stoichiometry.

The thickness of the pellet was adjusted based on the known sample composition and tabulated total neutron scattering cross-section values. The aim was to achieve the ratio of single to multiple scattering in the order of 1%, a value that is appropriate for the multiple scattering signal correction procedure based on the Monte Carlo (MC) transport code that is routinely used for VESUVIO data analysis [31,91–93]. The incident VESUVIO neutron beam profile has a Gaussian-like shape characterized by a full-width-at-half-maximum between 3.7 cm and 4.5 cm, depending upon the energy of detected neutrons (see Figure 3 in Ref. [94]). Exposing the sample directly to such an incident neutron beam would have introduced systematic errors in the transmission data analysis due to only a partial beam coverage by a pelletized sample of a diameter of 25 mm. For that reason, collimating inserts made out of boron carbide (B₄C) were placed into the incident neutron beam pipe, and the effective beam diameter after the collimation was reduced to 20 mm. For the treatment of neutron transmission data, a bespoke VesuvioTransmission algorithm, implemented in the MantidPlot computational environment, was employed [95–98].

The general VESUVIO setup for the NCS experiments has been described elsewhere [24,25,94]. The NCS spectra, recorded in the neutron time-of-flight (TOF) domain by 48 forward scattering detectors placed at scattering angles between 35 and 70 degrees, were analyzed. Apart from the recoil peaks of the atomic species present in the sample, the recorded TOF spectra contained the recoil peak of aluminum from the sample container and a series of unresolved peaks from the sample environment. Thus, two sets of experiments were performed: (i) one for the sample and sample environment and (ii) one for the sample environment without the sample material present. The second set of data was then subtracted from the first one. The resultant difference spectra were assumed not to contain any contributions from the aluminum and the sample environment. As mentioned in Section 3.2, the relative phase composition of 4 wt.% of Pd in cWO₃ corresponds to the Pd/W ratio of 0.092. In the NCS technique, the ratio of the integral peak intensities, I(Pd)/I(W), can be obtained by multiplying the factor 0.092 by the ratio of the respective total bound scattering cross-section values, 4.48/4.6, which yields I(Pd)/I(W) equal 0.0896. Thus, no palladium signal was considered to contribute to the total NCS signal.

The difference spectra were assumed to consist of hydrogen, oxygen, and tungsten recoil peaks, all with underlying purely Gaussian nuclear momentum distributions (NMDs) with standard deviations σ (hereinafter NMD widths). The NMD widths of tungsten and oxygen were kept fixed during the fitting at the values calculated from the DFT simulations described in the subsection below. This part of the experimental NCS data analysis was inspired by our previous NCS results in tungstic acid, where the experimental values of NMD widths of oxygen and tungsten practically coincide with the DFT predictions [99]. Moreover, the ratio of the relative scattering intensities (areas under the recoil peaks) of tungsten and oxygen has been fixed using the ratio of their respective total bound scattering cross-section values, weighted by the ratio of the number of tungsten and oxygen atomic

species per formula unit in $c\text{WO}_3$. This technique, stoichiometric fixing of scattering intensities, has been frequently applied in NCS data analysis of solid-state systems and molecules [31,99–102].

Using these constraints, a multi-step self-consistent iterative algorithm, implemented in the MantidPlot computational environment, was employed [23–27,30,32,34,92,103–106]. In the first step of the analysis, data were fitted sequentially (detector-by-detector) in the TOF domain. Prior to fitting, regions of TOF, where Breit–Wigner resonance peaks were present due to resonant neutron absorption in tungsten, were masked. The fits produced sets of relative scattering peak intensities and peak width values that were averaged. The average values of these parameters were then used to calculate the shapes of signals due to multiple scattering (MS) in the sample and sample-dependent gamma background (GB). The MS and GB signals were then subtracted sequentially from the total signals, and the corrected data were fitted again to obtain more precise fitted recoil peak signals of oxygen and tungsten. The fitted recoil peaks of oxygen and tungsten were then subtracted sequentially from the total signals, and the recoil peaks of hydrogen were isolated. The isolated hydrogen recoil peaks were then sequentially transformed into the hydrogen longitudinal momentum domain, where they were focused and further analyzed.

2.4. *Ab Initio Modelling*

As explained in the Introduction, the values of the NCS observables were predicted using DFT-based HLD analysis for two hydrogen subsystems: (i) hydrogen-terminated beta-palladium hydride (including the H-species both on the surface and within the Pd lattice) and (ii) hydrogen in acid centers (OH⁺ groups) on the surface of the cubic phase of tungsten oxide. In both cases, periodic density functional theory (periodic-DFT) calculations were carried out using a plane wave basis set and pseudopotentials as implemented in the CASTEP code [107–109]. The generalized gradient approximation (GGA) Perdew–Burke–Ernzerhof (PBE) functional [107,110–114] was used. In both cases, the computational protocol consisted of two steps: (i) full geometry optimization of the internal atomic coordinates was performed until the magnitudes of the residual forces were not greater than 0.0025 eV/Å, followed by (ii) the calculation of the phonon modes and accompanying atomic displacements that were used to obtain the atom-projected VDOSes. The as-obtained (i.e., without further scaling of the frequencies) phonon mode frequencies were used to calculate the values of the NCS observables.

In the case of the first subsystem, the DFT computational study was an extension of previously published work on the effect of particle size, morphology, and support on the formation of palladium hydride in commercial catalysts [80]. Optimized norm-conserving pseudopotentials with a plane-wave cut-off energy of 1050 eV were used. Two different Monkhorst–Pack k-point grids were used, $15 \times 15 \times 15$ (120 k-points) and $16 \times 16 \times 1$ (30 k-points), for the bulk and the surface species, respectively.

In the case of the second subsystem, on-the-fly-generated pseudopotentials were used with a plane-wave cut-off energy of 630 eV. The Monkhorst–Pack k-point grid was generated according to the specified k-point separation of 0.07 \AA^{-1} . The geometry optimization was first performed on the bulk cubic WO_3 phase. Then, the bulk phase was cleaved along the (1,1,1) direction. Finally, H atoms were added to the surface, and the geometry of the entire structure was optimized again using a periodic box containing a 10 \AA -wide vacuum gap. Following the geometry optimization, atom-projected VDOSes were obtained using the finite-displacement method. The supercell was defined by a cut-off radius of 20 \AA . Only the Brillouin zone Γ point was used for the calculation of the VDOSes.

The following NCS observables were calculated based on the underlying atom-projected VDOSes. The NMD width, σ_M , (expressed in units of \AA^{-1}) is defined for each nuclear isotope with mass M according to the formula [24,25,40,43]:

$$\sigma_M^2(T) = \frac{2M}{3\hbar^2} \frac{3\hbar}{4} \int d\omega G_M(\omega) \omega \coth(\hbar\omega/2k_B T) \quad (1)$$

where k_B is the Boltzmann constant, T the temperature, and $G_M(\omega)$ (with ω expressed in units of meV) is the atom-projected VDOS obtained from the ab initio HLD calculation in the limit of 0 K and weighted by the Boltzmann population factor $\coth(\hbar\omega/2k_B T)$.

The value of the nuclear kinetic energy, E_k (expressed in units of meV) can then be calculated from the value of σ_M using the following formula:

$$E_k(T) = \frac{3\hbar^2\sigma_M^2(T)}{2M} \quad (2)$$

From the values of the NMD widths, σ_M , one can obtain the values of the force constants, k_M , (in units of eV Å⁻²) corresponding to the underlying potential of the mean force (PMFs), with the mean force function (MF) defined as the average force acting on an atomic particle by keeping all other particles in the system fixed [29]. In the case of an isotropic harmonic potential, the underlying NMD is described by a Gaussian, the MF is linear with atomic displacement, and the magnitude (absolute value) of the force constant can be calculated using the formula [29]:

$$k_M = \frac{2M}{3\hbar^2} k_B T \left(E_k(T) - \frac{3}{2} k_B T \right) \quad (3)$$

Despite the limitation of the Trotter approximation in the limit of zero K [29], Formula (3) has been successfully applied to the description of the mean force in polycrystalline and amorphous ice at 100 K [29] and in the investigation of the local dynamics of tungsten oxide-based glasses at RT [115].

3. Results and Discussion

3.1. Ab Initio Modelling

Figure 2 shows the results of the geometry optimization of the structure of the hydrogen-terminated beta-palladium hydride (left panel) and the cubic phase of tungsten oxide with hydrogen in acid centers (OH⁺ groups) (right panel). In the case of the first structure, the electronic density distribution is shown. For the second structure, the electronic density difference (EDD) distribution is overlaid with the optimized geometry. EDD has become a popular option in the analysis of DFT studies of systems exhibiting hydrogen spillover [116]. The EDD function has been calculated with respect to a linear combination of the electronic densities of non-interacting atoms and shows the changes in the electron distribution that are due to the formation of all the bonds in the system. As can be clearly seen in the figure, the formation of the O—H bond on the surface of the cWO₃ phase causes positive polarization of the hydrogen species. OH⁺ acid centers are formed on the surface with positively charged hydrogen species with O—H bond length in the order of 0.97 Å, in agreement with values reported in the literature [117].

Figure 3 shows the results of the ab initio periodic DFT-based HLD simulations. According to Equation (1), the second moment of any NMD is strongly biased towards the high-energy part of an apVDOS, as every mode of vibration contributes to the total kinetic energy, an amount that is proportional to its vibrational frequency. Thus, the biggest contribution to the hydrogen NMD width and kinetic energy will be from the modes at ca. 260 and 460 meV for hydrogen-terminated beta-palladium hydride and the cubic phase of tungsten oxide terminated with hydrogen in acid centers, respectively. In the case of heavier atomic species, the bulk of the contribution lies in the low-energy part of their respective apVDOSes, below 40 meV in the case of palladium and below 100 meV in the case of oxygen and tungsten. Consequently, the hydrogen NMD width and kinetic energy values will be much more influenced by the local vibrational modes, whereas their counterparts for the heavyweight nuclear species will be dictated more by the lattice modes. The values of the NMD width, KE, and FC for all constituent atomic species in both systems, calculated using Formulas (1)–(3), respectively, are listed in Table 1.

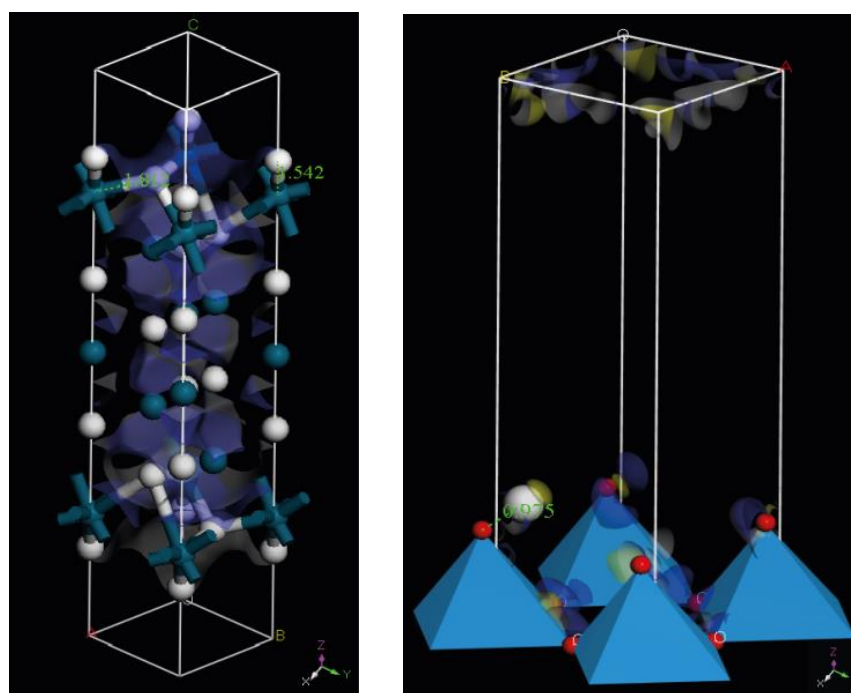


Figure 2. The results of the geometry optimization of the structure of the hydrogen-terminated beta-palladium hydride (**left panel**) and the cubic phase of tungsten oxide with hydrogen in acid centers (OH⁺ groups) (**right panel**). Interatomic distances are shown as green dashed lines and measured in units of Å. In the case of the hydrogen-terminated beta-palladium hydride, electronic density distribution is superimposed on the optimized structure. For the cubic phase of tungsten oxide with hydrogen in acid centers, the electronic density difference distribution is shown. The positive density difference is shown in yellow, while the negative one is in blue. See text for details.

It is clear from the inspection of Table 1 that the values of the mean force constant, representing effective binding in the local chemical environment, are quite different for different atomic species present in both systems under consideration. The average effective binding of hydrogen species in beta palladium hydride (including the component stemming from the surface termination) is three times weaker than the binding of palladium atoms in the lattice. The NMD width, KE, and FC values in the case of hydrogen in the beta phase of palladium hydride need to be contrasted with their counterparts in the case of free atomic hydrogen calculated based on the Maxwell–Boltzmann (MB) distribution. In the MB limit at 300K, NMD width equals 2.497 \AA^{-1} , the value of the KE is 38.78 meV, and there is no binding (FC is equal to zero). The hydrogen in the MB limit can be deemed to be a completely free, unconstrained particle [24,25]. The picture emerging from our DFT-based simulation of the nuclear hydrogen dynamics in the palladium hydride phase is in qualitative agreement with the overall view on the formation of the beta PdH phase (see Figure 10 in Ref. [80]). Namely, it is assumed that, at the lowest hydrogen content, only the surface threefold sites are occupied; the subsurface sites are then filled. As the hydrogen concentration increases, migration of the hydrogen into the bulk generates the alpha phase of PdH and eventually results in the formation of the beta PdH phase. The presence of the beta phase seems consistent with our experimental protocol involving a continuous gas flow exposure of the Pd/cWO₃ sample. Moreover, it seems that, in order for the alpha and beta PdH phases to be formed, the migration of the hydrogen species needs to be facilitated by a relatively low degree of binding of hydrogen in the lattice.

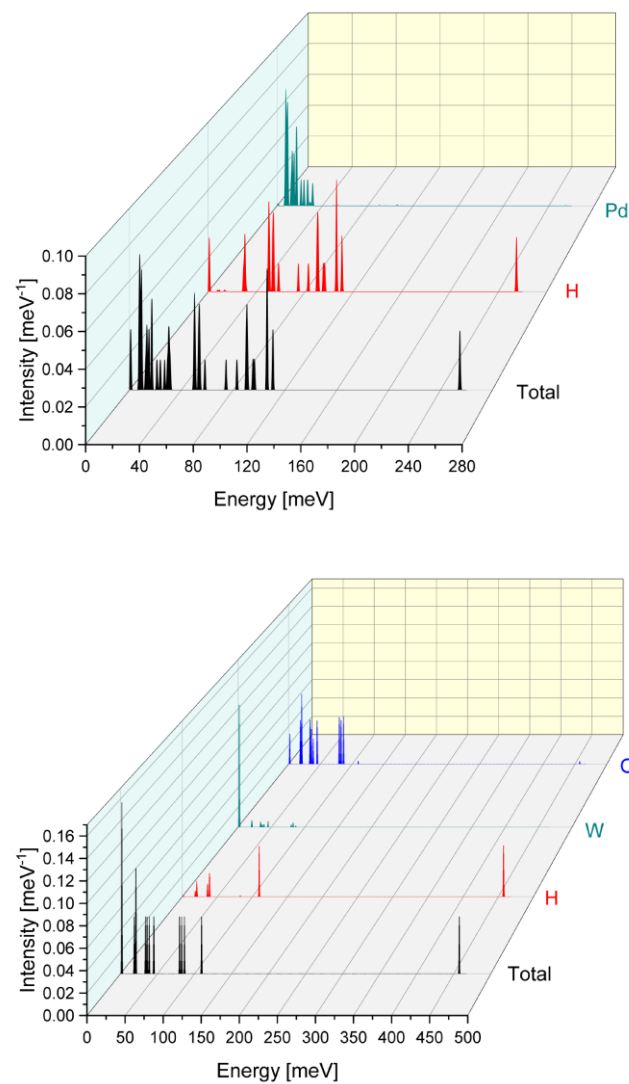


Figure 3. Calculated total and atom-projected VDOSes in the case of the hydrogen-terminated beta-palladium hydride and the cubic phase of tungsten oxide with hydrogen in acid centers (OH⁺ groups) are shown in the top and bottom panels, respectively. The labels H, Pd, O, and W refer to the hydrogen, palladium, oxygen, and tungsten-projected VDOSes. The label Total refers to the total VDOS.

Table 1. The theoretical (DFT-based) predictions of the NMD width, KE, and FC values for all constituent atomic species in the hydrogen-terminated beta-palladium hydride and the cubic phase of tungsten oxide terminated with hydrogen in acid centers (OH⁺ groups). The values of NMD width, KE, and FC have been calculated using Formulas (1)–(3), respectively.

Species	NMD Width [\AA^{-1}]	EK [meV]	FC [eV \AA^{-2}]
H in PdH	3.31	68.2	0.12
Pd	25.9	39.6	0.37
H in cWO ₃	4.91	149.7	0.46
O	11.6	52.8	0.93
W	35.6	43.2	3.30

In the case of the cubic phase of tungsten oxide terminated by the OH⁺ groups (acid centers), the value of the force constant for the hydrogen species is half of its counterpart for the oxygen and more than seven times smaller than the value of the force constant in the

case of tungsten. These values can be compared and contrasted with their experimental and theoretical counterparts obtained in our recent study on nuclear quantum dynamics in the tungstic acid, H_2WO_4 ($\text{WO}_3 \cdot \text{H}_2\text{O}$) [99]. Our Rietveld refinement procedure, augmented by a detailed neutron spectroscopic and DFT study, has revealed that the structure of $\text{WO}_3 \cdot \text{H}_2\text{O}$ is characterized by distorted octahedral units formed by tungsten atoms coordinated by five oxygen atoms and a water molecule. These octahedra share four corners in the equatorial plane to form sheets with water intercalated in between (see Figure 2 in Ref. [99]). In the case of the cubic phase of the WO_3 , the octahedral units formed by tungsten atoms coordinated by five oxygen atoms are not distorted. The different local chemical environments of tungsten and oxygen dictate different values of the NCS observables. The experimental values of the NMD width of the oxygen and tungsten in the tungstic acid are in very good agreement with the period DFT predictions (see Figure 7 in Ref. [99]). The NMD width values of oxygen and tungsten in the tungstic acid are ca 12.5 \AA^{-1} and 37 \AA^{-1} , respectively. Thus, it may be that the presence of a small degree of octahedral distortion in H_2WO_4 induces additional strains and stresses on the chemical bonds between tungsten and oxygen atoms, which is reflected in a higher degree of local binding of these atomic species, compared to their counterparts in Pd/cWO_3 . The NCS technique, when applied to the hydrogen in the hydroxyl groups, is a very potent tool for the differentiation between the tetrahedral local hydrogen bonding geometry and strong confinement-induced quasi-two dimensional arrangement of hydrogen-bonded molecules (see Figure 6 in Ref. [99]). As evidenced by the results of our ab initio periodic DFT geometry optimization presented above, the hydroxyl groups of the acid centers (OH^+), forming the hydrogen-terminated surface of the cubic phase of tungsten oxide, have O—H bond lengths only ca. 2% longer than O—H bond length in an isolated water molecule in vacuum (0.9572 \AA , see Ref. [118]). However, the simulated value of the NMD width of H in the O—H group on the surface of the cWO_3 is 4.91 \AA^{-1} . Given that the entire scale of NMD widths for protons in solid state systems and molecules spans between 3 and 5 \AA^{-1} [24,25,30], this value needs to be treated as much larger than 4.72 \AA^{-1} , which is its counterpart in bulk liquid water at RT [26]. This difference can, however, be explained by the fact that the formation of the network of hydrogen bonds in bulk water weakens (and lengthens) the covalent O—H bonds, thereby decreasing the value of the NMD width and FC of proton in this bond [26].

3.2. Characterization

Figure 4 shows the HRTEM image of the sample. One can clearly see the individual palladium nanocrystallites with diameters varying between 6 and 8 nm and their counterparts for the cubic phase of WO_3 compacted together to form the underlying base for the decoration with palladium.

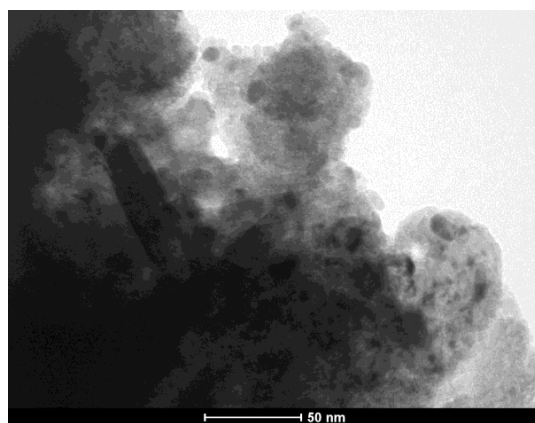


Figure 4. HRTEM images of the Pd/cWO_3 catalyst.

The XRD pattern of the same system is shown in Figure 5. The goodness-of-fit (GoF) and the weighted profile R-factor (Rwp) values are 7.12 and 5.22%, respectively. The

two-phase refinement confirms the cubic space group assignment for $c\text{WO}_3$ and Pd (space groups Pm-3m and Fm-3m , respectively) and the relative phase composition of 4 wt.% of Pd in $c\text{WO}_3$, assumed upon the material preparation, which corresponds to the Pd/W ratio of 0.092. Moreover, visible broadening of the Bragg peaks is observed, which stems from the microcrystalline nature of both phases. The average nanocrystal sizes inferred from the refinement are in agreement with the HRTEM image analysis results.

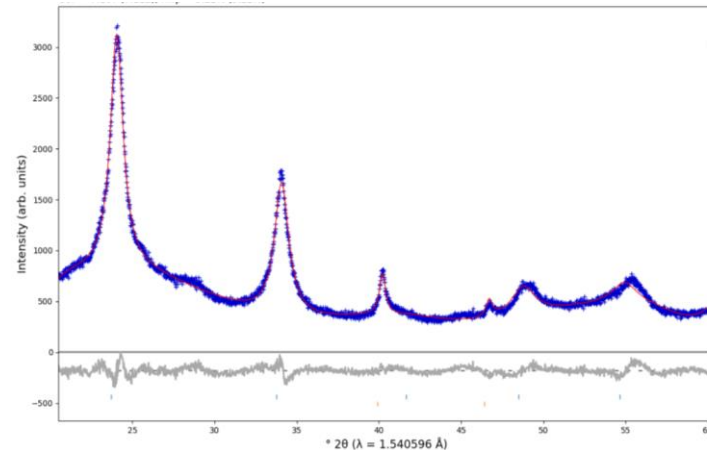


Figure 5. XRD pattern of the Pd/ $c\text{WO}_3$ sample (blue cross markers), together with the Rietveld fit (solid red line) and the residual (grey line in the bottom panel). Blue and orange vertical tick marks indicate reflections from the $c\text{WO}_3$ and Pd phases, respectively.

3.3. Neutron Scattering Measurements

Neutron transmission data are plotted as a function of the incident neutron energy at VESUVIO in Figure 6. The Pd/ $c\text{WO}_3$ sample transmission, corresponding to the plateau of the transmission curve for incident neutron energy values in the region of 100 eV, has a value of 0.87, in agreement with the initial estimate calculated based on the known sample number density, thickness, composition, and the values of the tabulated total free scattering cross sections for all constituent nuclei (according to the method outlined in Refs. [106,119,120]). This value corresponds to the ratio of single to multiple scattering in the order of 1%, which is suitable for using multiple scattering signal correction procedures based on the Monte Carlo (MC) transport code routinely used for VESUVIO data analysis.

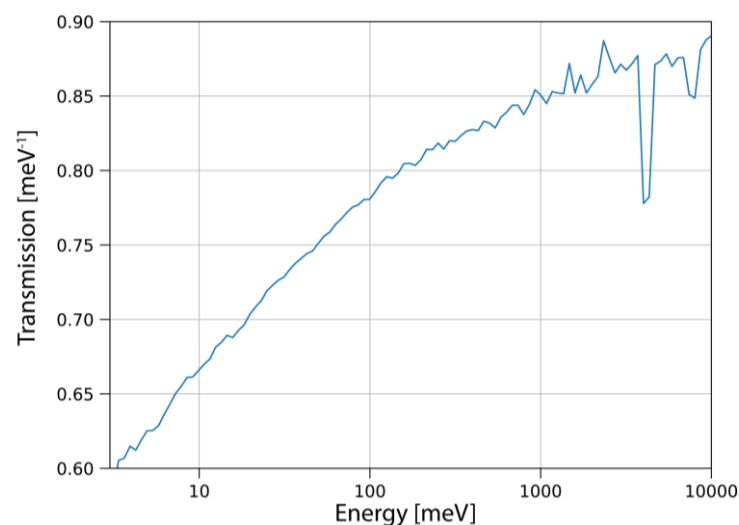


Figure 6. Neutron transmission of the Pd/ $c\text{WO}_3$ sample plotted as a function of incident neutron energy at VESUVIO.

Figure 7 shows the total neutron response of the Pd/cWO₃ sample focused in the TOF domain. A good quality fit has been achieved. The TOF region (marked as the red-shaded area in the plot), between 200 and 350 microseconds, represents the total signal due to Compton scattering off all three types of hydrogen species present in the sample.

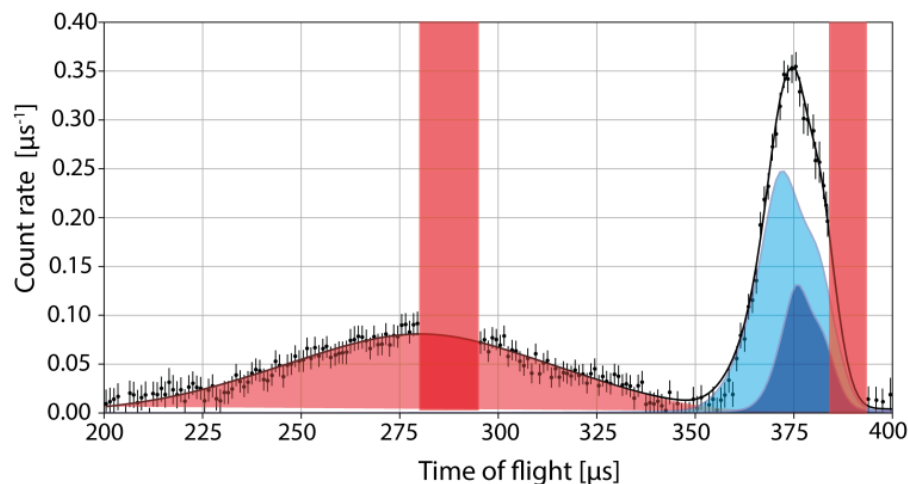


Figure 7. The total neutron response of the Pd/cWO₃ sample focused in the TOF domain. Black markers with error bars depict data. The solid black line represents the total fit to the focused data. Colored shaded areas represent the fitted focused recoil peak of hydrogen (red), oxygen (blue), and tungsten (cyan). The red-shaded rectangular areas depict data regions masked in fitting to exclude signals coming from the neutron-gamma resonances of tungsten. See text for details.

It can be clearly seen that there is a minimal degree of overlap between this signal and the rest of the signal due to the recoil peaks of oxygen and tungsten, a prerequisite for the good-quality analysis of the total hydrogen in the proton longitudinal momentum domain. As mentioned in Section 2.3, during the exposure of Pd/WO₃ to a flow of hydrogen at isothermal conditions on VESUVIO, the stoichiometry of the sample increased from Pd/cWO₃ towards Pd/H_{0.53}WO₃ bronze. The neutron Compton peak analysis in the time-of-flight domain confirms this stoichiometry. Namely, the H/W ratio obtained from the fitted integral intensities of the H and W recoil peaks shown in Figure 7 is 0.50 ± 0.03.

The total hydrogen NCS signal, transformed and focused on the longitudinal momentum domain (using the West-scaling variable [24,25], hereinafter referred to as y), is shown in Figure 8. As described above, our strategy has been to decompose the total signal in three distinct components: (i) the contribution from the momentum distribution of the hydrogen species present in the beta phase of PdH, (ii) the contribution from the hydrogen in OH+ acid centers present on the surface of the cubic phase of WO₃, and (iii) the contribution from the hydrogen species inside the H_xWO₃ bronze. The NMD widths of protons in the first two components were fixed in fitting at values obtained from the DFT simulations, as described in Section 3.1. Moreover, the ratio of relative contributions of the first and third components has been fixed, assuming that it is proportional to the ratio of the metallic phase of palladium to the cubic phase of tungsten oxide, as assumed in preparation, confirmed by XRD. Thus, the only free parameters in the analysis of data shown in Figure 8 are the NMD width of the hydrogen species inside the H_xWO₃ bronze and the relative contribution of these species, measured in units of the total signal. Such a heavily constrained fitting procedure allows for precise determination of the NMD width and relative contribution of the most elusive hydrogen species, the atomic hydrogen resulting from the spillover process. The fitting results are summarized in Table 2.

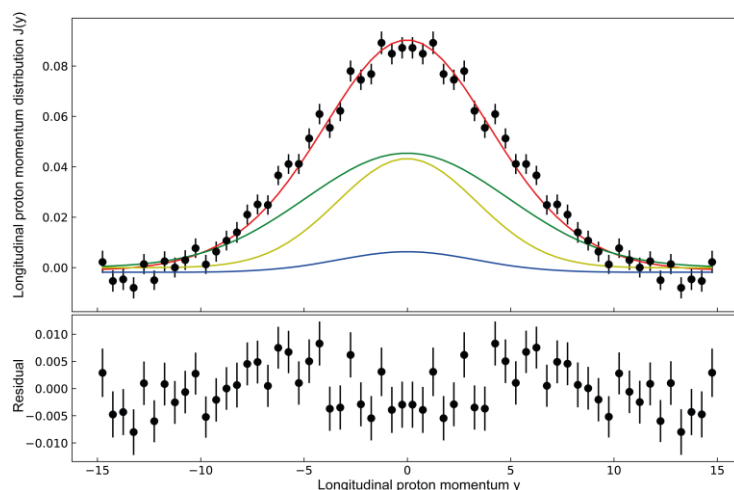


Figure 8. The total hydrogen NCS signal transformed and focused on the longitudinal momentum domain. The solid black markers, together with error bars, represent experimental data. The solid red line represents the total fit to the total hydrogen longitudinal proton momentum distribution. The solid blue line depicts the contribution from the momentum distribution of the hydrogen species present in the beta phase of PdH. The solid dark green line shows the contribution from the hydrogen in OH⁺ acid centers present on the surface of the cubic phase of WO₃. The solid light green lines represent the contribution of the hydrogen species inside the H_xWO₃ bronze. See text for details.

Table 2. The fitting results of the total hydrogen NCS signal are color-coded according to the color-coding in Figure 8. For details, see the text and Figure 8 caption.

Species	Contribution	NMD Width [\AA^{-1}]
H in PdH	0.0678 \pm 0.004	3.31 *
H in cWO ₃	0.5638 \pm 0.081	4.91 *
H in H _x WO ₃	0.3684 \pm 0.072	3.37 \pm 0.02

* Values fixed from the results of the DFT modeling.

As can be seen from Table 2, the component of the total hydrogen momentum distribution representing the hydrogen species inside the H_xWO₃ bronze (and thus the hydrogen stemming from the spillover process) is about one-third of the total signal, six times more than the contribution from the hydrogen in the beta phase of palladium hydride, and ca. 65% of the contribution from the hydrogen in OH⁺ acid centers present on the surface of the cubic phase of WO₃. This result reflects the morphology of the sample (see Figure 2), whereby the cubic phase of WO₃, due to its microcrystalline nature, provides a high surface-to-volume ratio and thus can accommodate more hydrogen on its surface than the bronze phase can accommodate in its bulk.

The NMD width of the hydrogen momentum distribution representing the hydrogen species inside the H_xWO₃ bronze equals 3.37 \pm 0.02 \AA^{-1} . This value corresponds to the value of the KE of 70.6 \pm 0.8 meV and the value of the MF of 0.16 \pm 0.01 eV \AA^{-2} . These values place the local binding strength of this pool of hydrogen species close to the hydrogen in the beta phase of palladium hydride. It should be noted that both these values are also quite close to the value (calculated from the MB distribution) for the free, unconstrained atomic hydrogen at RT (2.497 \AA^{-1}). These values seem physically meaningful since hydrogen species migrating from the surface towards the bulk phase of the bronze should exhibit a great deal of mobility.

As mentioned in the Introduction, two competing models seem to account for the properties of the hydrogen-intercalated tungsten trioxide [82]: (i) the model in which hydrogen is believed to remain in WO₃ as hydroxide and (ii) and the model in which hydrogen can form water with oxygen from WO₃ and leave the now substoichiometric

crystal. In a recent study of hydrogen in tungsten trioxide by membrane photoemission and density functional theory modeling [82], the authors provided compelling evidence that the hydrogen-induced coloration of tungsten trioxide can be accounted for using the second model. This model is consistent with the so-called proton polaron model of the hydration of oxygen-deficient metal-oxide proton conductors [83]. In this model, the hydration causes the filling of oxygen vacancies and the formation of hydroxyl groups with interstitial structural protons rotating around the oxygen in localized motion. Thermal activation triggers the delocalization of the protons by jumping to adjacent oxygen ions, constituting proton conductivity. Around RT, the conduction process is still essentially a quantum-mechanical phenomenon animated by metal-oxide and hydroxyl stretching modes and localized rotational motion of the protons around the oxygen atoms [83]. This model seems consistent with our picture of the local hydrogen dynamics inside the tungsten trioxide bulk phase. Namely, a ‘near-MB’ momentum distribution is much more consistent with delocalized hydrogen species performing ‘inter-octahedra transfer’ modulated by the metal-oxide and hydroxyl stretching motion than with a scenario in which hydrogen remains in WO_3 as hydroxide. In this latter case, the OH stretching vibrational mode would have dominated the hydrogen momentum distribution. A good approximation of such a hypothetical situation is provided by our DFT simulation of the hydrogen motion in the OH groups terminating the tungsten oxide surface, with the value of the width of the momentum distribution of 4.91 \AA^{-1} , much higher than 3.37 \AA^{-1} obtained from the NCS experiment for the hydrogen in the bulk tungsten oxide phase.

Our NCS results for the hydrogen momentum distribution representing the hydrogen species inside the H_xWO_3 bronze are also consistent with the results of a recent theoretical study of the local binding of the hydrogen species on the surface of the palladium catalyst and inside the bronze. The high mobility of H inside the WO_3 lattice was identified with low calculated diffusion barriers for several selected migration pathways [81]. The highest barrier for diffusion inside the bulk tungsten trioxide phase, calculated in this study, was 230 meV, and diffusion pathways were dissected into a series of jumps and rotations of hydrogen species around the oxygen atoms in the lattice, in agreement with the proton polaron model described above. Catalyst design for electrocatalytic hydrogen evolution reaction (HER) is guided by the classic “volcano” plot, in which neither too strong nor too weak adsorption of active hydrogen species on the catalyst surface is recognized as the criterion for efficient HER electrocatalysts since this state can facilitate both hydrogen adsorption and desorption [116,121]. Moreover, both hydrogen and deuterium nuclear magnetic resonance (NMR) studies have evidenced different pools of hydrogen in systems similar to Pd/cWO_3 , including weakly physisorbed hydrogen species on metal and support surfaces [49].

4. Conclusions

In summary, we have performed a comprehensive characterization of nuclear quantum dynamics and local binding of three hydrogen pools in the Pd/cWO_3 system: (i) hydrogen-terminated beta-palladium hydride, (ii) hydrogen in acid centers (OH+ groups) on the surface of the cubic phase of tungsten oxide, and (iii) quasi-free atomic hydrogen inside the saturated hydrogen bronze resulting from the spillover process.

Our characterization protocol consists of a unique combination of broadband neutron spectroscopic tools (neutron Compton scattering and incident neutron-dependent transmission), augmented with structural characterization and DFT modeling.

The deconvolution of the total longitudinal proton momentum distribution of the hydrogen into contributions from the three aforementioned hydrogen pools reveals that the local binding strength of hydrogen inside the saturated hydrogen bronze resulting from the spillover process is close to the hydrogen in the beta phase of palladium hydride. Thus, hydrogen species in both pools can be termed quasi-free, with the values of nuclear momentum distribution width, nuclear kinetic energy, and force constant of the underlying

potential of the mean force close to those of free, unconstrained hydrogen atomic species in a gas of non-interacting particles described by the Maxwell–Boltzmann distribution.

Our description of the quasi-free hydrogen species inside the bulk phase of tungsten trioxide is consistent with the proton polaron model of the hydration of oxygen-deficient metal-oxide proton conductors. In this model, protons are largely delocalized at temperatures around RT, and their diffusion is animated by metal-oxide and hydroxyl stretching motion and localized rotation around oxygen atoms.

The presented methodology offers an interesting alternative to the existing methodology to characterize hydrogen species in the context of the spillover phenomenon, such as scanning tunneling microscopy (STM), temperature-programmed desorption (TPD), in situ X-ray absorption spectroscopy, NMR, Raman spectroscopy, and low-energy electron diffraction. The presented methodology, when combined with selective deuteration and more advanced modeling techniques such as ab initio molecular dynamics or path integral molecular dynamics, will pave the way for more sophisticated characterization protocols of catalytic systems in which hydrogen spillover occurs.

Author Contributions: Conceptualization, M.K., E.L. and S.F.P.; methodology, M.K., S.F.P., G.R., G.I., E.L., M.J.G., I.d.S. and R.K.; software, M.K., S.F.P., I.d.S., M.J.G. and G.R.; validation, E.L., S.F.P., G.I., I.d.S., M.J.G., G.R., K.D., R.K. and M.K.; formal analysis, E.L., S.F.P., I.d.S., M.J.G., G.R., K.D. and M.K.; investigation, E.L., S.F.P., G.I. and M.K.; resources, E.L., M.K., R.K., S.F.P. and G.I.; data curation, M.K. and S.F.P.; writing—original draft preparation, M.K.; writing—review and editing, M.K., E.L., S.F.P., I.d.S., M.J.G., G.R., K.D. and R.K.; visualization, M.K. and S.F.P.; supervision, M.K.; project administration, M.K. and E.L. All authors have read and agreed to the published version of the manuscript.

Funding: This research was funded by the UK Science and Technology Facilities Council via direct access proposal (RB1920033, VESUVIO).

Data Availability Statement: All data that support the findings of this study are included within the article. Raw experimental data are archived at DOI: 10.5286/ISIS.E.RB1920033.

Acknowledgments: The authors gratefully acknowledge the ISIS Facility for the provision of neutron beam time. EL acknowledges the assistance of Microscal Energy Technology Ltd. (Thatcham, UK).

Conflicts of Interest: The authors declare no conflict of interest.

References

1. Kosydar, R.; Kolodziej, M.; Lalik, E.; Gurgul, J.; Mordarski, G.; Drelinkiewicz, A. The role of hydrogen bronzes in the hydrogenation of polyfunctional reagents: Cinnamaldehyde, furfural and 5-hydroxymethylfurfural over Pd/H_xWO₃ and Pd/H_xMoO₃ catalysts. *Int. J. Hydrogen Energy* **2022**, *47*, 2347–2365. [[CrossRef](#)]
2. Mobtakeri, S.; Habashyani, S.; Gür, E. Highly Responsive Pd-Decorated MoO₃ Nanowall H₂ Gas Sensors Obtained from In-Situ-Controlled Thermal Oxidation of Sputtered MoS₂ Films. *ACS Appl. Mater. Interfaces* **2022**, *14*, 25741–25752. [[CrossRef](#)]
3. Rojas, S.; Roble, M.; Morales-Ferreiro, J.O.; Diaz-Droguett, D.E. Comparative study on the hydrogen storage capacity of crystalline and amorphous nanomaterials of MoO₃: Effect of a catalytic Pd capping. *Ionics* **2018**, *24*, 3101–3111. [[CrossRef](#)]
4. Xu, K.; Liao, N.; Xue, W.; Zhou, H. First principles investigation on MoO₃ as room temperature and high temperature hydrogen gas sensor. *Int. J. Hydrogen Energy* **2020**, *45*, 9252–9259. [[CrossRef](#)]
5. Fei, S.X.; Han, B.; Li, L.L.; Mei, P.; Zhu, T.; Yang, M.; Cheng, H.S. A study on the catalytic hydrogenation of N-ethylcarbazole on the mesoporous Pd/MoO₃ catalyst. *Int. J. Hydrogen Energy* **2017**, *42*, 25942–25950. [[CrossRef](#)]
6. Kolodziej, M.; Drelinkiewicz, A.; Lalik, E.; Gurgul, J.; Duraczynska, D.; Kosydar, R. Activity/selectivity control in Pd/H_xMoO₃ catalyzed cinnamaldehyde hydrogenation. *Appl. Catal. A-Gen.* **2016**, *515*, 60–71. [[CrossRef](#)]
7. Kolodziej, M.; Lalik, E.; Colmenares, J.C.; Lisowski, R.; Gurgul, J.; Duraczynska, D.; Drelinkiewicz, A. Physicochemical and catalytic properties of Pd/MoO₃ prepared by the sonophotodeposition method. *Mater. Chem. Phys.* **2018**, *204*, 361–372. [[CrossRef](#)]
8. Kuwahara, Y.; Okada, M.; Ge, H.; Yamashita, H. Hydrodeoxygenation of Aromatic Ketones under Mild Conditions over Pd-loaded Hydrogen Molybdenum Bronze with Plasmonic Features. *Chem. Lett.* **2022**, *51*, 166–169. [[CrossRef](#)]
9. Matsuda, T.; Ohno, T.; Sakagami, H.; Takahashi, N. Reduction of MoO₃ to porous molybdenum oxides and its catalytic properties for alkane isomerization. *J. Jpn. Pet. Inst.* **2007**, *50*, 229–239. [[CrossRef](#)]
10. Moberg, D.R.; Thibodeau, T.J.; Amar, F.G.; Frederick, B.G. Mechanism of Hydrodeoxygenation of Acrolein on a Cluster Model of MoO₃. *J. Phys. Chem. C* **2010**, *114*, 13782–13795. [[CrossRef](#)]

11. Thibodeau, T.J.; Canney, A.S.; DeSisto, W.J.; Wheeler, M.C.; Amar, F.G.; Frederick, B.G. Composition of tungsten oxide bronzes active for hydrodeoxygenation. *Appl. Catal. A-Gen.* **2010**, *388*, 86–95. [[CrossRef](#)]
12. Xi, Y.J.; Chen, Z.X.; Kiat, V.G.W.; Huang, L.; Cheng, H.S. On the mechanism of catalytic hydrogenation of thiophene on hydrogen tungsten bronze. *Phys. Chem. Chem. Phys.* **2015**, *17*, 9698–9705. [[CrossRef](#)] [[PubMed](#)]
13. Shaikh, S.F.; Ghule, B.G.; Shinde, P.V.; Raut, S.D.; Gore, S.K.; Ubaidullah, M.; Mane, R.S.; Al-Enizi, A.M. Continuous hydrothermal flow-inspired synthesis and ultra-fast ammonia and humidity room-temperature sensor activities of WO₃ nanobricks. *Mater. Res. Express* **2020**, *7*, 015076. [[CrossRef](#)]
14. Loopstra, B.O.; Rietveld, H.M. Further refinement of the structure of WO₃. *Acta Crystallogr. Sect. B* **1969**, *25*, 1420–1421. [[CrossRef](#)]
15. Shaikh, S.F.; Kalanur, S.S.; Mane, R.S.; Joo, O.S. Monoclinic WO₃ nanorods-rutile TiO₂ nanoparticles core-shell interface for efficient DSSCs. *Dalton Trans.* **2013**, *42*, 10085–10088. [[CrossRef](#)] [[PubMed](#)]
16. Urretavizcaya, G.; Tonus, F.; Gaudin, E.; Bobet, J.L.; Castro, F.J. Formation of tetragonal hydrogen tungsten bronze by reactive mechanical alloying. *J. Solid State Chem.* **2007**, *180*, 2785–2789. [[CrossRef](#)]
17. Yamaguchi, O.; Tomihisa, D.; Kawabata, H.; Shimizu, K. Formation and Transformation of Wo₃ Prepared from Alkoxide. *J. Am. Ceram. Soc.* **1987**, *70*, C94–C96. [[CrossRef](#)]
18. Figlarz, M. Soft Chemistry–Thermodynamic and Structural Aspects. *Soft Chem. Routes New Mater. Chim. Douce* **1994**, *152*, 55–68. [[CrossRef](#)]
19. Guery, C.; Choquet, C.; Dujeancourt, F.; Tarascon, J.M.; Lassegues, J.C. Infrared and X-ray studies of hydrogen intercalation in different tungsten trioxides and tungsten trioxide hydrates. *J. Solid State Electrochem.* **1997**, *1*, 199–207. [[CrossRef](#)]
20. Cao, J.; Luo, B.D.; Lin, H.L.; Xu, B.Y.; Chen, S.F. Thermodecomposition synthesis of WO₃/H₂WO₄ heterostructures with enhanced visible light photocatalytic properties. *Appl. Catal. B Environ.* **2012**, *111*, 288–296. [[CrossRef](#)]
21. Drelinkiewicz, A.; Lalik, E.; Kosydar, R.; Pacuła, A.; Góral-Kurbiel, M.; Kołodziej, M.; Szumelda, T. *Catalytic Processes Using Bio-Resources. Palladium Catalysts Reactivity Modified by Tungsten Hydrogen Bronzes*; Detailed Research Report of Jerzy Haber Institute of Catalysis and Surface Chemistry; Polish Academy of Sciences: Cracow, Poland, 2017; p. 9.
22. Mayers, J.; Reiter, G. The VESUVIO electron volt neutron spectrometer. *Meas. Sci. Technol.* **2012**, *23*, 045902. [[CrossRef](#)]
23. Senesi, R.; Andreani, C.; Bowden, Z.; Colognesi, D.; Degiorgi, E.; Fielding, A.L.; Mayers, J.; Nardone, M.; Norris, J.; Praitano, M.; et al. VESUVIO: A novel instrument for performing spectroscopic studies in condensed matter with eV neutrons at the ISIS facility. *Phys. B* **2000**, *276*, 200–201. [[CrossRef](#)]
24. Andreani, C.; Krzystyniak, M.; Romanelli, G.; Senesi, R.; Fernandez-Alonso, F. Electron-volt neutron spectroscopy: Beyond fundamental systems. *Adv. Phys.* **2017**, *66*, 1–73. [[CrossRef](#)]
25. Andreani, C.; Senesi, R.; Krzystyniak, M.; Romanelli, G.; Fernandez-Alonso, F. Chapter 7–Atomic Quantum Dynamics in Materials Research. In *Experimental Methods in the Physical Sciences*; Fernandez-Alonso, F., Price, D.L., Eds.; Academic Press: New York, NY, USA, 2017; Volume 49, pp. 403–457.
26. Andreani, C.; Senesi, R.; Krzystyniak, M.; Romanelli, G.; Fernandez-Alonso, F.F. Experimental studies of nuclear quantum effects in condensed matter: The case of water. *Riv. Nuovo. Cimento.* **2018**, *41*, 291–340. [[CrossRef](#)]
27. Krzystyniak, M.; Romanelli, G.; Fabian, M.; Gutmann, M.; Festa, G.; Arcidiacono, L.; Gigg, M.; Druzbecki, K.; Andreani, C.; Senesi, R.; et al. VESUVIO plus: The Current Testbed for a Next-generation Epithermal Neutron Spectrometer. *J. Phys. Conf. Ser.* **2018**, *1021*, 012026. [[CrossRef](#)]
28. Seel, A.G.; Krzystyniak, M.; Fernandez-Alonso, F. The VESUVIO Spectrometer Now and When? *J. Phys. Conf. Ser.* **2014**, *571*, 012006. [[CrossRef](#)]
29. Parmentier, A.; Andreani, C.; Romanelli, G.; Shephard, J.J.; Salzmann, C.G.; Senesi, R. Hydrogen mean force and anharmonicity in polycrystalline and amorphous ice. *Front. Phys.* **2018**, *13*, 136101. [[CrossRef](#)]
30. Andreani, C.; Colognesi, D.; Mayers, J.; Reiter, G.; Senesi, R. Measurement of momentum distribution of lightatoms and molecules in condensed matter systems using inelastic neutron scattering. *Adv. Phys.* **2005**, *54*, 377–469. [[CrossRef](#)]
31. Wallis, J.; Kruth, A.; da Silva, I.; Krzystyniak, M. Nuclear dynamics in BaZr_{0.7}Ce_{0.2}Y_{0.1}O_{3–δ} proton conductor as observed by neutron diffraction and Compton scattering. *J. Phys. Commun.* **2020**, *4*, 045004. [[CrossRef](#)]
32. Krzystyniak, M.; Druzbecki, K.; Rudić, S.; Fabian, M. Positional, isotopic mass and force constant disorder in molybdate glasses and their parent metal oxides as observed by neutron diffraction and Compton scattering. *J. Phys. Commun.* **2020**, *4*, 095027. [[CrossRef](#)]
33. Druzbecki, K.; Krzystyniak, M.; Hollas, D.; Kapil, V.; Slavicek, P.; Romanelli, G.; Fernandez-Alonso, F. Hydrogen dynamics in solid formic acid: Insights from simulations with quantum colored-noise thermostats. *J. Phys. Conf. Ser.* **2018**, *1055*, 012003. [[CrossRef](#)]
34. Krzystyniak, M.; Druzbecki, K.; Romanelli, G.; Gutmann, M.J.; Rudic, S.; Imberti, S.; Fernandez-Alonso, F. Nuclear dynamics and phase polymorphism in solid formic acid. *Phys. Chem. Chem. Phys.* **2017**, *19*, 9064–9074. [[CrossRef](#)] [[PubMed](#)]
35. Krzystyniak, M.; Druzbecki, K.; Fernandez-Alonso, F. Nuclear dynamics in the metastable phase of the solid acid caesium hydrogen sulfate. *Phys. Chem. Chem. Phys.* **2015**, *17*, 31287–31296. [[CrossRef](#)] [[PubMed](#)]
36. Krzystyniak, M.; Seel, A.G.; Richards, S.E.; Gutmann, M.J.; Fernandez-Alonso, F. Mass-selective Neutron Spectroscopy Beyond the Proton. *J. Phys. Conf. Ser.* **2014**, *571*, 012002. [[CrossRef](#)]
37. Ceriotti, M.; Drechsel-Grau, C.; Fernandez-Alonso, F.; Greaves, N.; Krzystyniak, M.; Major, D.; Parmentier, A.; Salzmann, C.; Senesi, R.; Sturniolo, S.; et al. Discussion: Theoretical Horizons and Calculation. *J. Phys. Conf. Ser.* **2014**, *571*, 012013. [[CrossRef](#)]

38. Andreani, C.; Ceriotti, M.; Chass, G.; Drechsel-Grau, C.; Fernandez-Alonso, F.; Greaves, N.; Gidopoulos, N.; Krzystyniak, M.; Parmentier, A.; Refson, K.; et al. Discussion: Nuclear Quantum Dynamics—Protons and Beyond. *J. Phys. Conf. Ser.* **2014**, *571*, 012004. [[CrossRef](#)]
39. Krzystyniak, M.; Richards, S.E.; Seel, A.G.; Fernandez-Alonso, F. Mass-selective neutron spectroscopy of lithium hydride and deuteride: Experimental assessment of the harmonic and impulse approximations. *Phys. Rev. B* **2013**, *88*, 184304. [[CrossRef](#)]
40. Krzystyniak, M.; Fernandez-Alonso, F. Ab initio nuclear momentum distributions in lithium hydride: Assessing nonadiabatic effects. *Phys. Rev. B* **2011**, *83*, 134305. [[CrossRef](#)]
41. Krzystyniak, M.; Adams, M.A.; Lovell, A.; Skipper, N.T.; Bennington, S.M.; Mayers, J.; Fernandez-Alonso, F. Probing the binding and spatial arrangement of molecular hydrogen in porous hosts via neutron Compton scattering. *Faraday Discuss.* **2011**, *151*, 171–197. [[CrossRef](#)]
42. Krzystyniak, M.; Abdul-Redah, T. Proton momentum distribution in solid and liquid HF. *Phys. Rev. B* **2010**, *82*, 064301. [[CrossRef](#)]
43. Krzystyniak, M. Nuclear momentum distribution in solid and liquid HF from ab initio calculation. *J. Chem. Phys.* **2010**, *133*, 144505. [[CrossRef](#)] [[PubMed](#)]
44. Chen, S.; Yang, T.X.; Lu, H.; Liu, Y.A.; He, Y.F.; Li, Q.; Gao, J.X.; Feng, J.T.; Yan, H.; Miller, J.T.; et al. Increased Hydrogenation Rates in Pd/La-Al₂O₃ Catalysts by Hydrogen Transfer O(-La) Sites Adjacent to Pd Nanoparticles. *ACS Catal.* **2022**, *12*, 15696–15706. [[CrossRef](#)]
45. Gu, K.X.; Li, C.; Jiang, B.; Lin, S.; Guo, H. Short- and Long-Time Dynamics of Hydrogen Spillover from a Single Atom Platinum Active Site to the Cu(111) Host Surface. *J. Phys. Chem. C* **2022**, *126*, 17093–17101. [[CrossRef](#)]
46. Hulseley, M.J.; Fung, V.; Hou, X.D.; Wu, J.S.; Yan, N. Hydrogen Spillover and Its Relation to Hydrogenation: Observations on Structurally Defined Single-Atom Sites. *Angew. Chem. Int. Ed.* **2022**, *61*, e202208237. [[CrossRef](#)]
47. Jing, W.T.; Shen, H.; Qin, R.X.; Wu, Q.Y.; Liu, K.L.; Zheng, N.F. Surface and Interface Coordination Chemistry Learned from Model Heterogeneous Metal Nanocatalysts: From Atomically Dispersed Catalysts to Atomically Precise Clusters. *Chem. Rev.* **2022**, *123*, 5948–6002. [[CrossRef](#)] [[PubMed](#)]
48. Kamada, T.; Ueda, T.; Fukuura, S.; Yumura, T.; Hosokawa, S.; Tanaka, T.; Kan, D.S.K.; Shimakawa, Y. Ultralong Distance Hydrogen Spillover Enabled by Valence Changes in a Metal Oxide Surface. *J. Am. Chem. Soc.* **2023**, *145*, 1631–1637. [[CrossRef](#)]
49. Liu, K.R.; Hou, G.J.; Gao, P.; Nie, X.Z.; Bai, S.; Janik, M.J.; Zhang, Z.C. Evolution of multiple spillover hydrogen species on anatase titanium dioxide. *Cell Rep. Phys. Sci.* **2022**, *3*, 101190. [[CrossRef](#)]
50. Osada, W.; Tanaka, S.; Mukai, K.; Kawamura, M.; Choi, Y.; Ozaki, F.; Ozaki, T.; Yoshinobu, J. Elucidation of the atomic-scale processes of dissociative adsorption and spillover of hydrogen on the single atom alloy catalyst Pd/Cu(111). *Phys. Chem. Chem. Phys.* **2022**, *24*, 21705–21713. [[CrossRef](#)]
51. Shen, H.F.; Li, H.; Yang, Z.S.; Li, C.L. Magic of hydrogen spillover: Understanding and application. *Green Energy Environ.* **2022**, *7*, 1161–1198. [[CrossRef](#)]
52. Wang, X.Y.; Li, D.D.; Gao, Z.R.; Guo, Y.; Zhang, H.B.; Ma, D. The Nature of Interfacial Catalysis over Pt/NiAl₂O₄ for Hydrogen Production from Methanol Reforming Reaction. *J. Am. Chem. Soc.* **2022**, *145*, 905–918. [[CrossRef](#)]
53. Wang, Y.L.; Yin, H.B.; Dong, F.; Zhao, X.G.; Qu, Y.K.; Wang, L.X.; Peng, Y.; Wang, D.S.; Fang, W.; Li, J.H. N-Coordinated Cu-Ni Dual-Single-Atom Catalyst for Highly Selective Electrocatalytic Reduction of Nitrate to Ammonia. *Small* **2023**, *19*, 2207695. [[CrossRef](#)]
54. Yue, G.C.; Yu, Y.; Li, S.; Li, H.K.; Gao, S.W.; Wang, Y.Q.; Guo, W.; Wang, N.; Li, X.L.; Cui, Z.M.; et al. Boosting Chemoselective Hydrogenation of Nitroaromatic via Synergy of Hydrogen Spillover and Preferential Adsorption on Magnetically Recoverable Pt@Fe₂O₃. *Small* **2023**, *19*, 2207918. [[CrossRef](#)] [[PubMed](#)]
55. Vallejo, E. An hydrogen adsorption study on graphene-based surfaces with core-shell type catalysts. *Carbon Lett.* **2023**, *33*, 823–832. [[CrossRef](#)]
56. Schmitz, G.; Schnieder, B. Adaptive regularized Gaussian process regression for application in the context of hydrogen adsorption on graphene sheets. *J. Comput. Chem.* **2023**, *44*, 732–744. [[CrossRef](#)]
57. Sun, J.K.; Jiang, S.C.; Zhao, Y.L.; Wang, H.L.; Zhai, D.; Deng, W.Q.; Sun, L. First-principles study of CO₂ hydrogenation to formic acid on single-atom catalysts supported on SiO₂. *Phys. Chem. Chem. Phys.* **2022**, *24*, 19938–19947. [[CrossRef](#)] [[PubMed](#)]
58. Injongkol, Y.; Khemthong, P.; Yodsins, N.; Wongnongwa, Y.; Sosa, N.; Youngjan, S.; Butburee, T.; Rungtaweeworant, B.; Kiatphuengporn, S.; Wittayakun, J.; et al. Combined in situ XAS and DFT studies on the role of Pt in zeolite-supported metal catalysts for selective n-hexane isomerization. *Fuel* **2022**, *314*, 123099. [[CrossRef](#)]
59. Zhao, G.C.; Qiu, Y.Q.; Liu, C.G. A systematic theoretical study of hydrogen activation, spillover and desorption in single-atom alloys. *Appl. Catal. A-Gen.* **2021**, *610*, 117948. [[CrossRef](#)]
60. Dadayan, A.K.; Borisov, Y.A.; Zolotarev, Y.A.; Myasoedov, N.F. Modeling Hydrogen Spillover on Oxide Catalytic Centers. *Russ. J. Phys. Chem. A+* **2021**, *95*, 944–948. [[CrossRef](#)]
61. Lykhach, Y.; Kubat, J.; Neitzel, A.; Tsud, N.; Vorokhta, M.; Skala, T.; Dvorak, F.; Kosto, Y.; Prince, K.C.; Matolin, V.; et al. Charge transfer and spillover phenomena in ceria-supported iridium catalysts: A model study. *J. Chem. Phys.* **2019**, *151*, 2204703. [[CrossRef](#)]
62. Guo, J.H.; Li, X.D.; Liu, H.Y.; Li, S.J.; Chen, G. Combined Density Functional Theory and Kinetic Monte Carlo Study of Hydrogen Spillover on Fluorine-Decorating Covalent Organic Frameworks. *J. Phys. Chem. C* **2019**, *123*, 15935–15943. [[CrossRef](#)]

63. Doudin, N.; Yuk, S.F.; Marcinkowski, M.D.; Nguyen, M.T.; Liu, J.C.; Wang, Y.; Novotny, Z.; Kay, B.D.; Li, J.; Glezakou, V.A.; et al. Understanding Heterolytic H₂ Cleavage and Water-Assisted Hydrogen Spillover on Fe₃O₄(001)-Supported Single Palladium Atoms. *Acs Catal.* **2019**, *9*, 7876–7887. [CrossRef]
64. Ren, B.H.; Li, J.D.; Wen, G.B.; Ricardez-Sandoval, L.; Croiset, E. First-Principles Based Microkinetic Modeling of CO₂ Reduction at the Ni/SDC Cathode of a Solid Oxide Electrolysis Cell. *J. Phys. Chem. C* **2018**, *122*, 21151–21161. [CrossRef]
65. Guo, J.H.; Liu, D.D.; Li, X.D.; Liu, H.Y.; Chen, G. Pt-4, Pd-4, Ni-4, and Ti-4 catalyzed hydrogen spillover on penta-graphene for hydrogen storage: The first-principles and kinetic Monte Carlo study. *Int. J. Hydrogen Energy* **2018**, *43*, 2247–2255. [CrossRef]
66. Shin, H.; Choi, M.; Kim, H. A mechanistic model for hydrogen activation, spillover, and its chemical reaction in a zeolite-encapsulated Pt catalyst. *Phys. Chem. Chem. Phys.* **2016**, *18*, 7035–7041. [CrossRef] [PubMed]
67. Lucci, F.R.; Darby, M.T.; Mattera, M.F.G.; Ivimey, C.J.; Therrien, A.J.; Michaelides, A.; Stamatakis, M.; Sykes, E.C.H. Controlling Hydrogen Activation, Spillover, and Desorption with Pd-Au Single-Atom Alloys. *J. Phys. Chem. Lett.* **2016**, *7*, 480–485. [CrossRef]
68. Guo, J.H.; Cheng, X.L.; Li, S.J.; Chen, G. Theoretical Study of a Bridging-Spillover Mechanism in Covalent Organic Frameworks on Pt-6 and Pt-4 Cluster Models. *J. Phys. Chem. C* **2016**, *120*, 17153–17164. [CrossRef]
69. Blanco-Rey, M.; Juaristi, J.I.; Alducin, M.; Lopez, M.J.; Alonso, J.A. Is Spillover Relevant for Hydrogen Adsorption and Storage in Porous Carbons Doped with Palladium Nanoparticles? *J. Phys. Chem. C* **2016**, *120*, 17357–17364. [CrossRef]
70. Juarez-Mosqueda, R.; Mavrandonakis, A.; Kuc, A.B.; Pettersson, L.G.M.; Heine, T. Theoretical analysis of hydrogen spillover mechanism on carbon nanotubes. *Front. Chem.* **2015**, *3*, 2. [CrossRef]
71. Choi, S.; Jeong, K.J.; Park, J.Y.; Lee, Y.S. Computational Study of Hydrogen Chemisorption on a Multi-Phenyl Organic Linker as a Model of Hydrogen Spillover on Metal-Organic Frameworks. *B Korean Chem. Soc.* **2015**, *36*, 777–783. [CrossRef]
72. Choi, M.; Yook, S.; Kim, H. Hydrogen Spillover in Encapsulated Metal Catalysts: New Opportunities for Designing Advanced Hydroprocessing Catalysts. *ChemCatChem* **2015**, *7*, 1048–1057. [CrossRef]
73. Nishihara, H.; Ittisanronnachai, S.; Itoi, H.; Li, L.X.; Suzuki, K.; Nagashima, U.; Ogawa, H.; Kyotani, T.; Ito, M. Experimental and Theoretical Studies of Hydrogen/Deuterium Spillover on Pt-Loaded Zeolite-Templated Carbon. *J. Phys. Chem. C* **2014**, *118*, 9551–9559. [CrossRef]
74. Ma, L.; Zhang, J.M.; Xu, K.W. Hydrogen storage on nitrogen induced defects in palladium-decorated graphene: A first-principles study. *Appl. Surf. Sci.* **2014**, *292*, 921–927. [CrossRef]
75. Liu, X.Y.; He, J.; Yu, J.X.; Li, Z.X.; Fan, Z.Q. Theoretical study of molecular hydrogen and spillover hydrogen storage on two-dimensional covalent-organic frameworks. *Chin. Phys. B* **2014**, *23*, 067303. [CrossRef]
76. Karlicky, F.; Lepetit, B.; Lemoine, D. Quantum modelling of hydrogen chemisorption on graphene and graphite. *J. Chem. Phys.* **2014**, *140*, 124702. [CrossRef] [PubMed]
77. Marcinkowski, M.D.; Jewell, A.D.; Stamatakis, M.; Boucher, M.B.; Lewis, E.A.; Murphy, C.J.; Kyriakou, G.; Sykes, E.C.H. Controlling a spillover pathway with the molecular cork effect. *Nat. Mater.* **2013**, *12*, 523–528. [CrossRef]
78. Hao, S.Q.; Sholl, D.S. First-Principles Models of Facilitating H₂ Transport through Metal Films Using Spillover. *J. Phys. Chem. C* **2013**, *117*, 1217–1223. [CrossRef]
79. Mitchell, P.C.H.; Ramirez-Cuesta, A.J.; Parker, S.F.; Tomkinson, J. Inelastic neutron scattering in spectroscopic studies of hydrogen on carbon-supported catalysts-experimental spectra and computed spectra of model systems. *J. Mol. Struct.* **2003**, *651*, 781–785. [CrossRef]
80. Parker, S.F.; Walker, H.C.; Callear, S.K.; Grunewald, E.; Petzold, T.; Wolf, D.; Mobus, K.; Adam, J.; Wieland, S.D.; Jimenez-Ruiz, M.; et al. The effect of particle size, morphology and support on the formation of palladium hydride in commercial catalysts. *Chem. Sci.* **2019**, *10*, 480–489. [CrossRef]
81. Xi, Y.J.; Zhang, Q.F.; Cheng, H.S. Mechanism of Hydrogen Spillover on WO₃(001) and Formation of H_xWO₃ (x = 0.125, 0.25, 0.375, and 0.5). *J. Phys. Chem. C* **2014**, *118*, 494–501. [CrossRef]
82. Billeter, E.; Sterzi, A.; Sambalova, O.; Wick-Joliat, R.; Grazioli, C.; Coreno, M.; Cheng, Y.Q.; Ramirez-Cuesta, A.J.; Borgschulte, A. Hydrogen in tungsten trioxide by membrane photoemission and density functional theory modeling. *Phys. Rev. B* **2021**, *103*, 205304. [CrossRef]
83. Braun, A.; Chen, Q.L. Experimental neutron scattering evidence for proton polaron in hydrated metal oxide proton conductors. *Nat. Commun.* **2017**, *8*, 15830. [CrossRef] [PubMed]
84. Hjelm, A.; Granqvist, C.G.; Wills, J.M. Electronic structure and optical properties of WO₃, LiWO₃, NaWO₃, and HWO₃. *Phys. Rev. B* **1996**, *54*, 2436–2445. [CrossRef] [PubMed]
85. Johansson, M.B.; Kristiansen, P.T.; Duda, L.; Niklasson, G.A.; Osterlund, L. Band gap states in nanocrystalline WO₃ thin films studied by soft X-ray spectroscopy and optical spectrophotometry. *J. Phys.-Condens. Matter* **2016**, *28*, 475802. [CrossRef] [PubMed]
86. Leng, X.; Pereiro, J.; Strle, J.; Dubuis, G.; Bollinger, A.T.; Gozar, A.; Wu, J.; Litombe, N.; Panagopoulos, C.; Pavuna, D.; et al. Insulator to metal transition in WO₃ induced by electrolyte gating. *npj Quantum Mater.* **2017**, *2*, 35. [CrossRef]
87. Saenger, M.F.; Hoing, T.; Hofmann, T.; Schubert, M. Polaron transitions in charge intercalated amorphous tungsten oxide thin films. *Phys. Status Solidi A-Appl. Mater. Sci.* **2008**, *205*, 914–917. [CrossRef]
88. Saenger, M.F.; Hoing, T.; Robertson, B.W.; Billa, R.B.; Hofmann, T.; Schubert, E.; Schubert, M. Polaron and phonon properties in proton intercalated amorphous tungsten oxide thin films. *Phys. Rev. B* **2008**, *78*, 245205. [CrossRef]
89. Lalik, E.; Mirek, R.; Rakoczy, J.; Groszek, A. Microcalorimetric study of sorption of water and ethanol in zeolites 3A and 5A. *Catal. Today* **2006**, *114*, 242–247. [CrossRef]

90. Irvine, G.J.; Demmel, F.; Playford, H.Y.; Carins, G.; Jones, M.O.; Irvine, J.T.S. Geometric Frustration and Concerted Migration in the Superionic Conductor Barium Hydride. *Chem. Mater.* **2022**, *34*, 9934–9944. [[CrossRef](#)]
91. Krzystyniak, M.; Romanelli, G.; Fernandez-Alonso, F. Non-destructive quantitation of hydrogen via mass-resolved neutron spectroscopy. *Analyst* **2019**, *144*, 3936–3941. [[CrossRef](#)]
92. Romanelli, G.; Hower, B.; Krzystyniak, M.; Gigg, M.; Tolchenov, R.; Mukhopadhyay, S.; Fernandez-Alonso, F. Data analysis of neutron Compton scattering experiments using MANTID. *J. Phys. Conf. Ser.* **2018**, *1055*, 012016. [[CrossRef](#)]
93. Mayers, J.; Fielding, A.L.; Senesi, R. Multiple scattering in deep inelastic neutron scattering: Monte Carlo simulations and experiments at the ISIS eVS inverse geometry spectrometer. *Nucl. Instrum. Meth. A* **2002**, *481*, 454–463. [[CrossRef](#)]
94. Romanelli, G.; Krzystyniak, M.; Senesi, R.; Raspino, D.; Boxall, J.; Pooley, D.; Moorby, S.; Schooneveld, E.; Rhodes, N.; Andreani, C. Characterisation of the incident beam and current diffraction capabilities on the VESUVIO spectrometer. *Meas. Sci. Technol.* **2017**, *28*, 095501. [[CrossRef](#)]
95. Capelli, S.C.; Romanelli, G. An effective hydrogen scattering cross section for time-of-flight neutron experiments with simple organic molecules. *J. Appl. Crystallogr.* **2019**, *52*, 1233–1237. [[CrossRef](#)]
96. Damian, J.I.M.; Dawidowski, J.; Granada, R.J.; Cantargi, F.; Romanelli, G.; Helman, C.; Krzystyniak, M.; Skoro, G.; Roubtsov, D. Experimental validation of the temperature behavior of the ENDF/B-VIII.0 thermal scattering kernel for light water. *Epj Web Conf.* **2020**, *239*, 14001. [[CrossRef](#)]
97. Martellucci, M.; Romanelli, G.; Valeri, S.; Cottone, D.; Andreani, C.; Senesi, R. The neutron cross section of barite-enriched concrete for radioprotection shielding in the range 1 meV–1 keV. *Eur. Phys. J. Plus* **2021**, *136*, 259. [[CrossRef](#)]
98. Robledo, J.I.; Dawidowski, J.; Damian, J.I.M.; Skoro, G.; Bovo, C.; Romanelli, G. Measurement of neutron total cross sections at the VESUVIO spectrometer. *Nucl. Instrum. Meth. A* **2020**, *971*, 164096. [[CrossRef](#)]
99. Lalik, E.; Druzicki, K.; Irvine, G.; Gutmann, M.; Rudic, S.; Manuel, P.; Petricek, V.; Krzystyniak, M. Interplay between Local Structure and Nuclear Dynamics in Tungstic Acid: A Neutron Scattering Study. *J. Phys. Chem. C* **2021**, *125*, 23864–23879. [[CrossRef](#)]
100. Krzystyniak, M.; Syrykh, G.; Stolyarov, A.; Sadykov, R.A.; Armstrong, J.; da Silva, I.; Romanelli, G.; Fernandez-Alonso, F. Mass-selective neutron spectroscopy of glassy versus polycrystalline structures in binary mixtures of beryllium and zirconium. *J. Phys. Conf. Ser.* **2018**, *1055*, 012004. [[CrossRef](#)]
101. Krzystyniak, M.; Syrykh, G.; Stolyarov, A.; Sadykov, R.A.; Romanelli, G. Force constant disorder in the Ni₄₄Nb₅₆ bulk metallic glass as observed by deep inelastic neutron scattering augmented by isotopic substitution. *Phys. Scr.* **2022**, *97*, 065702. [[CrossRef](#)]
102. Syrykh, G.F.; Stolyarov, A.A.; Krzystyniak, M.; Romanelli, G.; Sadykov, R.A. Temperature Dependence of the Kinetic Energy in the Zr₄₀Be₆₀ Amorphous Alloy. *Jetp. Lett+* **2017**, *105*, 591–594. [[CrossRef](#)]
103. Fernandez-Alonso, F.; Price, D.L. *Neutron Scattering: Applications in Biology, Chemistry and Materials Science*; Academic Press, an Imprint of Elsevier: Cambridge, MA, USA, 2017; p. 753.
104. Jackson, S.; Krzystyniak, M.; Seel, A.G.; Gigg, M.; Richards, S.E.; Fernandez-Alonso, F. VESUVIO Data Analysis Goes MANTID. *J. Phys. Conf. Ser.* **2014**, *571*, 012009. [[CrossRef](#)]
105. Krzystyniak, M.; Gutmann, M.J.; Refson, K.; Romanelli, G.; Rudic, S.; Capelli, S.C.; Fortes, D.; Magdysyuk, O.; Damin, J.I.M.; Maciel-Pereira, G. Nuclear quantum dynamics in Hexamethylenetetramine and its deuterated counterpart: A DFT-augmented neutron study. *Phys. Scr.* **2023**, *98*, 025707. [[CrossRef](#)]
106. Witek, M.; Krzystyniak, M.; Romanelli, G.; Witzczak, T. Glass Transition in Rice Pasta as Observed by Combined Neutron Scattering and Time-Domain NMR. *Polymers* **2021**, *13*, 2426. [[CrossRef](#)] [[PubMed](#)]
107. Milman, V.; Refson, K.; Clark, S.J.; Pickard, C.J.; Yates, J.R.; Gao, S.P.; Hasnip, P.J.; Probert, M.I.J.; Perlov, A.; Segall, M.D. Electron and vibrational spectroscopies using DFT, plane waves and pseudopotentials: CASTEP implementation. *J. Mol. Struct.-Theochem.* **2010**, *954*, 22–35. [[CrossRef](#)]
108. Clark, S.J.; Segall, M.D.; Pickard, C.J.; Hasnip, P.J.; Probert, M.J.; Refson, K.; Payne, M.C. First principles methods using CASTEP. *Z. Krist.* **2005**, *220*, 567–570. [[CrossRef](#)]
109. Segall, M.D.; Lindan, P.J.D.; Probert, M.J.; Pickard, C.J.; Hasnip, P.J.; Clark, S.J.; Payne, M.C. First-principles simulation: Ideas, illustrations and the CASTEP code. *J. Phys.-Condens. Matter* **2002**, *14*, 2717–2744. [[CrossRef](#)]
110. Peng, H.W.; Perdew, J.P. Rehabilitation of the Perdew-Burke-Ernzerhof generalized gradient approximation for layered materials. *Phys. Rev. B* **2017**, *95*, 081105. [[CrossRef](#)]
111. Pedroza, L.S.; da Silva, A.J.R.; Capelle, K. Gradient-dependent density functionals of the Perdew-Burke-Ernzerhof type for atoms, molecules, and solids. *Phys. Rev. B* **2009**, *79*, 201106. [[CrossRef](#)]
112. Ropo, M.; Kokko, K.; Vitos, L. Assessing the Perdew-Burke-Ernzerhof exchange-correlation density functional revised for metallic bulk and surface systems. *Phys. Rev. B* **2008**, *77*, 195445. [[CrossRef](#)]
113. Xu, X.; Goddard, W.A. The extended Perdew-Burke-Ernzerhof functional with improved accuracy for thermodynamic and electronic properties of molecular systems. *J. Chem. Phys.* **2004**, *121*, 4068–4082. [[CrossRef](#)]
114. Ernzerhof, M.; Scuseria, G.E. Assessment of the Perdew-Burke-Ernzerhof exchange-correlation functional. *J. Chem. Phys.* **1999**, *110*, 5029–5036. [[CrossRef](#)]
115. Krzystyniak, M.; Druzicki, K.; Tolnai, I.; Fabian, M. Local structure and dynamics of tungsten oxide-based glasses: Insights from concurrent neutron diffraction and Compton scattering. *J. Phys. Commun.* **2021**, *5*, 075013. [[CrossRef](#)]

116. Li, J.Y.; Hu, J.; Zhang, M.K.; Gou, W.Y.; Zhang, S.; Chen, Z.; Qu, Y.Q.; Ma, Y.Y. A fundamental viewpoint on the hydrogen spillover phenomenon of electrocatalytic hydrogen evolution. *Nat. Commun.* **2021**, *12*, 3502. [[CrossRef](#)]
117. Wang, J.Q.; Su, Y.C.; Xu, J.; Ye, C.H.; Deng, F. Acid sites and oxidation center in molybdena supported on tin oxide as studied by solid-state NMR spectroscopy and theoretical calculation. *Phys. Chem. Chem. Phys.* **2006**, *8*, 2378–2384. [[CrossRef](#)] [[PubMed](#)]
118. Sutton, L.E. *Tables of Interatomic Distances and Configuration in Molecules and Ions: Supplement 1956–1959*; Chemical Society: Cambridge, UK, 1965.
119. Palomino, L.A.R.; Dawidowski, J.; Helman, C.; Damian, J.I.M.; Romanelli, G.; Krzystyniak, M.; Rudic, S.; Cuello, G.J. Determination of the scattering cross section of calcium using the VESUVIO spectrometer. *Nucl. Instrum. Meth. A* **2019**, *927*, 443–450. [[CrossRef](#)]
120. Romanelli, G.; Onorati, D.; Ulpiani, P.; Cancelli, S.; Perelli-Cippo, E.; Damian, J.I.M.; Capelli, S.C.; Croci, G.; Muraro, A.; Tardocchi, M.; et al. Thermal neutron cross sections of amino acids from average contributions of functional groups. *J. Phys.-Condens. Matter* **2021**, *33*, 285901. [[CrossRef](#)] [[PubMed](#)]
121. Zheng, Y.; Jiao, Y.; Jaroniec, M.; Qiao, S.Z. Advancing the Electrochemistry of the Hydrogen-Evolution Reaction through Combining Experiment and Theory. *Angew. Chem. Int. Ed.* **2015**, *54*, 52–65. [[CrossRef](#)]

Disclaimer/Publisher’s Note: The statements, opinions and data contained in all publications are solely those of the individual author(s) and contributor(s) and not of MDPI and/or the editor(s). MDPI and/or the editor(s) disclaim responsibility for any injury to people or property resulting from any ideas, methods, instructions or products referred to in the content.